Data-Driven Quest for Two-Dimensional Non-van der Waals Materials
Supporting Information

Rico Friedrich,[1,2,*] Mahdi Ghorbani-Asl,[1] Stefano Curtarolo,[2,3] and Arkady V. Krasheninnikov[1,4]

[1] *Institute of Ion Beam Physics and Materials Research, Helmholtz-Zentrum Dresden-Rossendorf, 01328 Dresden, Germany*
[2] *Center for Autonomous Materials Design, Duke University, Durham, North Carolina 27708, USA*
[3] *Materials Science, Electrical Engineering, and Physics, Duke University, Durham NC, 27708, USA*
[4] *Department of Applied Physics, Aalto University, Aalto 00076, Finland*

(Dated: January 6, 2022)

I. Comparing exfoliation energies from different functionals

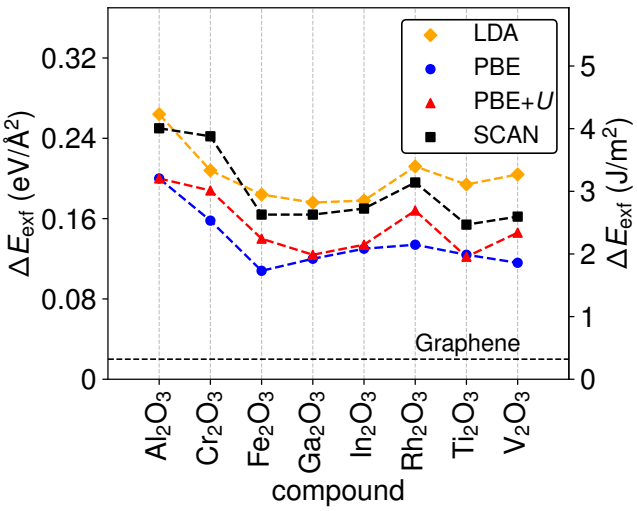

FIG. S1. **Exfoliation energies for binaries.** Exfoliation energies of investigated binary systems for different functionals. Note that in case of Al_2O_3 PBE+U reduces to PBE. As a reference, the exfoliation energy of graphene [1, 2] is indicated by the dashed horizontal black line. The dashed lines connecting the data points are visual guides.

In Fig. S1, the calculated exfoliation energies of the binary systems for four different functionals are summarized. All approaches show similar trends and sizes of the computed values with LDA mostly providing estimates on the upper while PBE yields values on the lower end. The biggest absolute deviation between the functionals of 88 meV/Å^2 is observed for V_2O_3 between LDA and PBE. It can thus be concluded that the calculation of exfoliation energies of these systems as energy differences between chemically similar bulk and 2D systems is rather insensitive to the choice of the functional. It can be performed efficiently within standard approximations.

II. Comparing exfoliation energies from relaxing different degrees of freedom

After obtaining the 2D facets of the binaries from the bulk parent structures, we considered three different approaches for optimizing the structural degrees of freedom: (i) performing only a static self-consistent electronic calculation, (ii) also relaxing the ionic positions in the cell and (iii) also relaxing the (in-plane) cell parameters. The first approach has been employed in the large scale screening of vdW 2D materials [2] since for these systems the weak inter-layer bonding does typically not give rise to strong relaxations. For the latter approach, the VASP option to relax the cell shape

* r.friedrich@hzdr.de

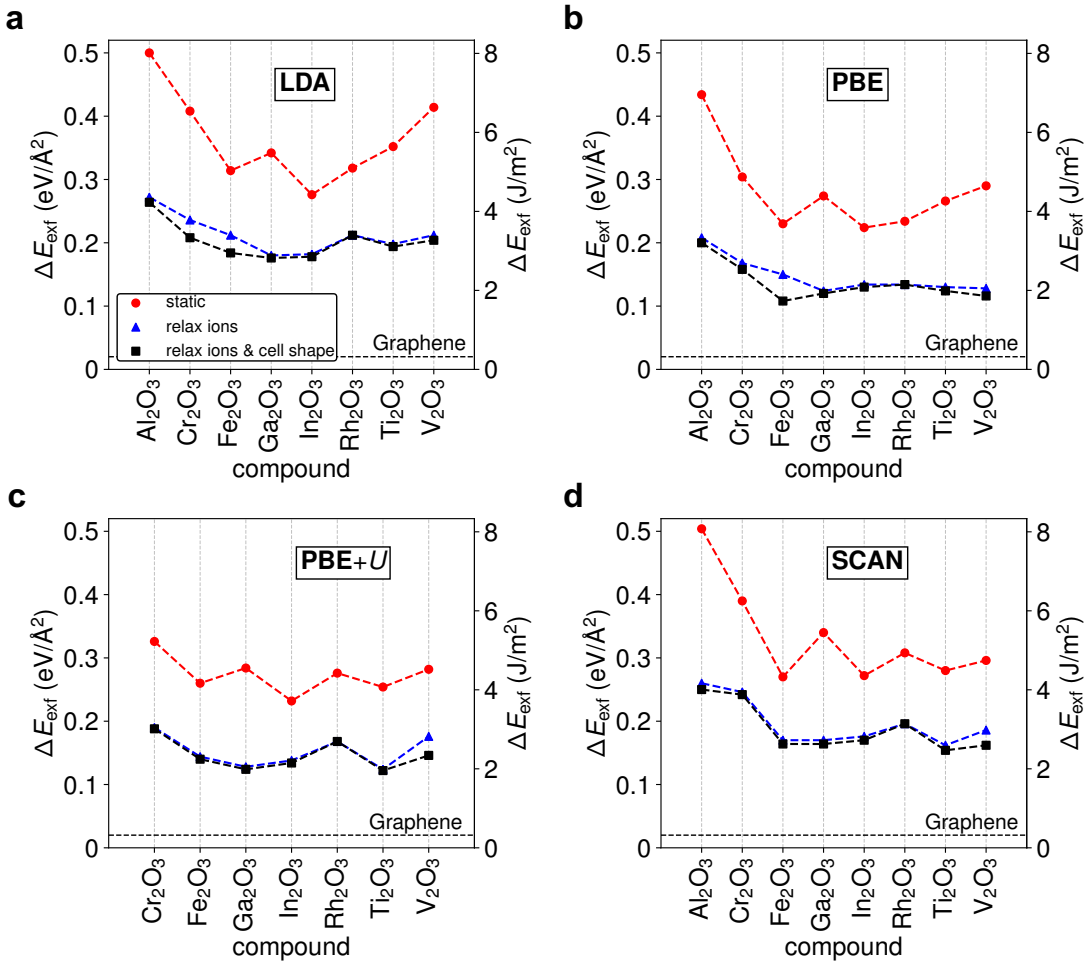

FIG. S2. **Exfoliation energies from relaxing different degrees of freedom.** Comparison of exfoliation energies calculated from only a static electronic calculation, a relaxation of the ionic positions as well as also relaxing the cell shape of the 2D systems for LDA (**a**), PBE (**b**), PBE+U (**c**), and SCAN (**d**). For PBE+U, the results for Al_2O_3 are not plotted as they are the same as for PBE. The dashed lines connecting the data points are visual guides.

was chosen to allow the in-plane lattice parameters and angles to relax while keeping the overall volume, including the large vacuum distances to the periodic images, constant. The results are visualized in Fig. S2 for all four considered functionals. In each case, the exfoliation energies are reduced by about a factor of two upon including ionic relaxations. Also relaxing the cell leads to only a minor additional energy gain of typically a few meV/Å^2. The largest energy gain upon cell relaxation is observed for Fe_2O_3 for PBE amounting to 42 meV/Å^2. In conclusion, while only performing a static calculation is not a reliable approximation for non-vdW 2D systems, the relaxation of ionic positions usually suffices to estimate their exfoliation energy. For the investigation of the ternary systems, we have decided to consider only the full relaxation including cell parameters in this study.

III. Comparing exfoliation energies for different terminations for ternary systems

Fig. S3 compares the exfoliation energies of the ternary 2D systems with different cation terminations. In general, the difference between the energetically preferred termination compared to the less stable one is substantial amounting to a factor of two to five for both functionals. The SCAN exfoliation energies are usually higher than the ones from PBE+U for both terminations. A special case is $GeMnO_3$. PBE+U yields the Mn-termination to be lower in energy while SCAN favors the Ge-termination. This qualitatively different behavior can be traced back to different oxidation numbers found by the approaches indicated by the charges and magnetic moments. While PBE+U finds Mn and Ge to be in oxidation states +2 and +4, respectively, SCAN yields the opposite. This can be assigned to the well known self-interaction error that has been pointed out to persist for this functional [3]. That SCAN gives a lower ΔE_{exf} than

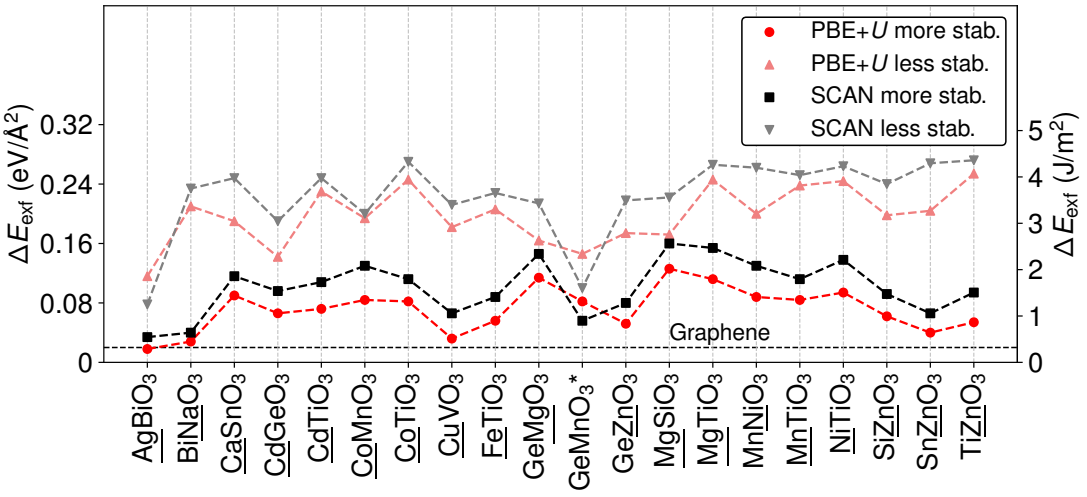

FIG. S3. **Exfoliation energies for different terminations for ternary systems.** The terminating elements for the energetically more stable slabs are underlined. In case of $GeMnO_3$ (marked by "*"), PBE+U favors Mn termination while for SCAN Ge termination is preferred. The dashed lines connecting the data points are visual guides.

PBE+U for the Bi terminated slabs for $AgBiO_3$ has likely a similar reason.

IV. Change of structural parameters for SCAN

As indicated in Fig. S4, also for SCAN the expansion of the in-plane lattice parameters correlates well with the thickness reduction of the slabs upon exfoliation.

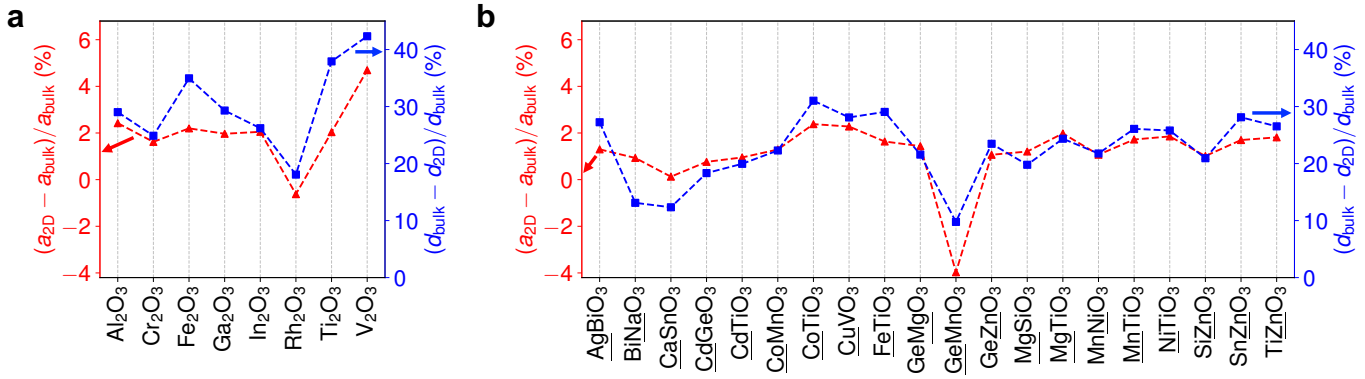

FIG. S4. **Modification of structural parameters.** Change of structural parameters for binary (**a**) and ternary (**b**) materials upon exfoliation as calculated with SCAN. The modification of the in-plane lattice parameter is indicated by the red curves (left y-axis) while the thickness change is given by the blue curves (right y-axis). The ternary data are for the energetically preferred slab termination. The dashed lines connecting the data points are visual guides.

V. Band structures

The band structures and corresponding densities of states (DOSs) of the bulk and 2D systems as obatined from PBE+U are presented in Figs. S5 to S32. A general oberservation is that, as expected, the bands show less dispersion for the 2D systems compared to their bulk counterparts due to the missing out of plane interaction. For the 2D sheets of Ti_2O_3 and V_2O_3, the hexagonal symmetry of the cell was slightly broken during the relaxation such that the automatic analysis of AFLOW finds a different k-path as for the other systems. Therefore, in these cases only the DOS is presented. For $AgBiO_3$ and $BiNaO_3$ linear band crossings at the K-point are observed hinting at potentially interesting topological features.

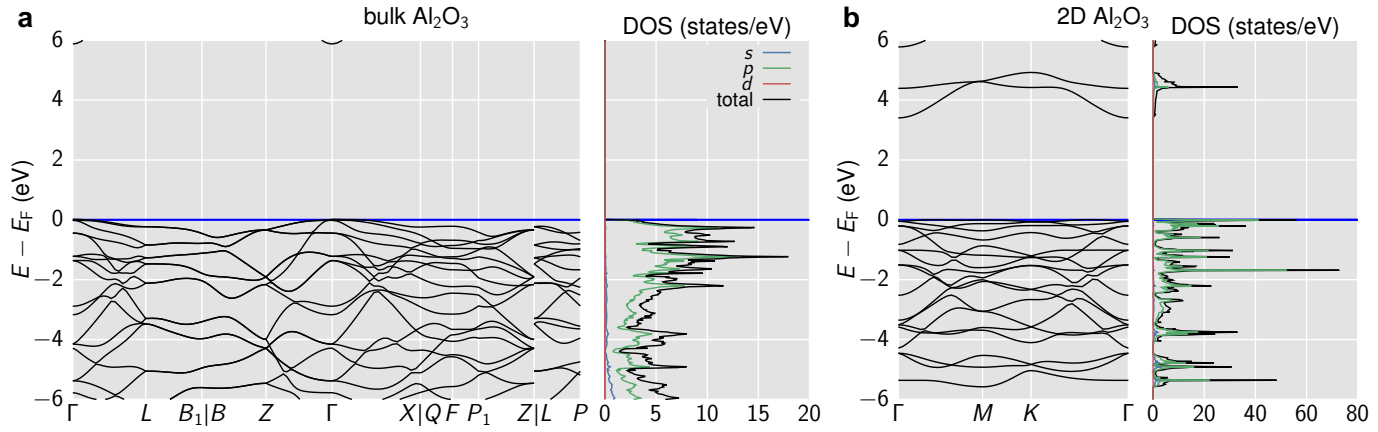

FIG. S5. Bandstructure and density of states for bulk (**a**) and 2D (**b**) Al_2O_3. The energies are aligned at the respective Fermi energy E_F.

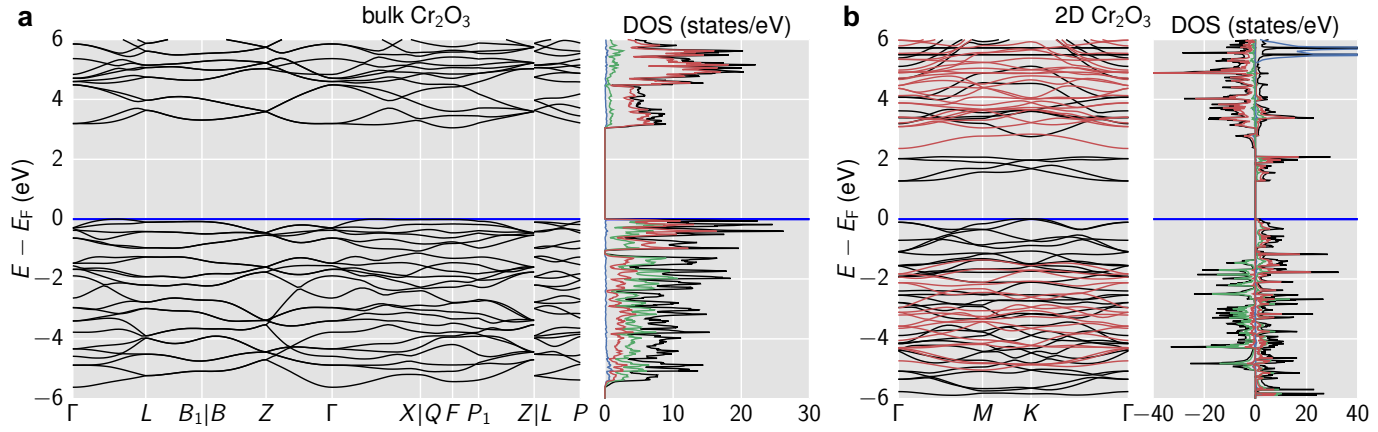

FIG. S6. Bandstructure and density of states for bulk (**a**) and 2D (**b**) Cr_2O_3. The energies are aligned at the respective Fermi energy E_F. For the spin polarized bandstructure, majority spin bands (positive DOS) are indicated in black while minority spin bands (negative DOS) are in red.

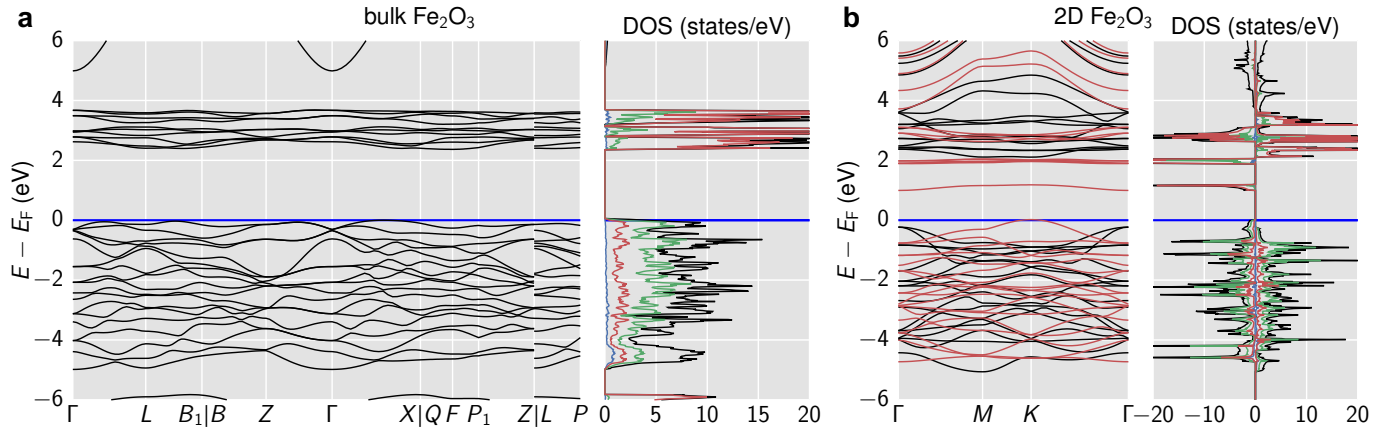

FIG. S7. Bandstructure and density of states for bulk (**a**) and 2D (**b**) Fe_2O_3. The energies are aligned at the respective Fermi energy E_F. For the spin polarized bandstructure, majority spin bands (positive DOS) are indicated in black while minority spin bands (negative DOS) are in red.

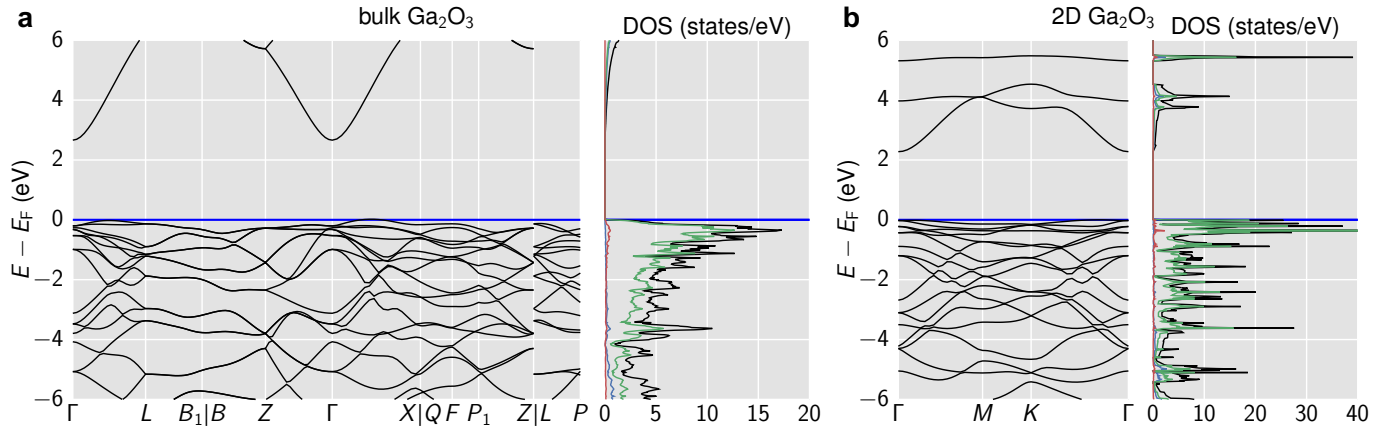

FIG. S8. Bandstructure and density of states for bulk (**a**) and 2D (**b**) Ga_2O_3. The energies are aligned at the respective Fermi energy E_F.

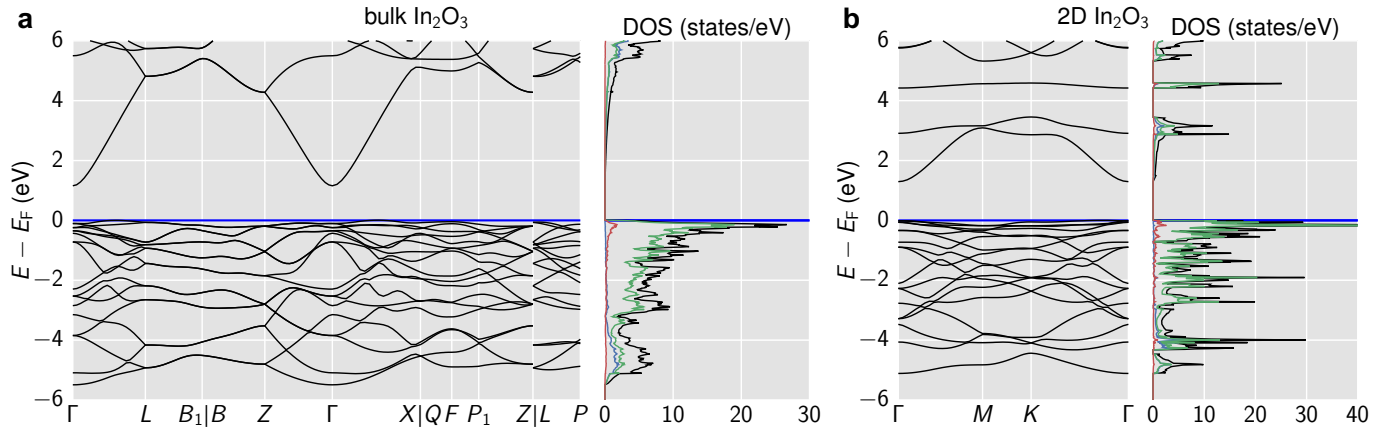

FIG. S9. Bandstructure and density of states for bulk (**a**) and 2D (**b**) In_2O_3. The energies are aligned at the respective Fermi energy E_F.

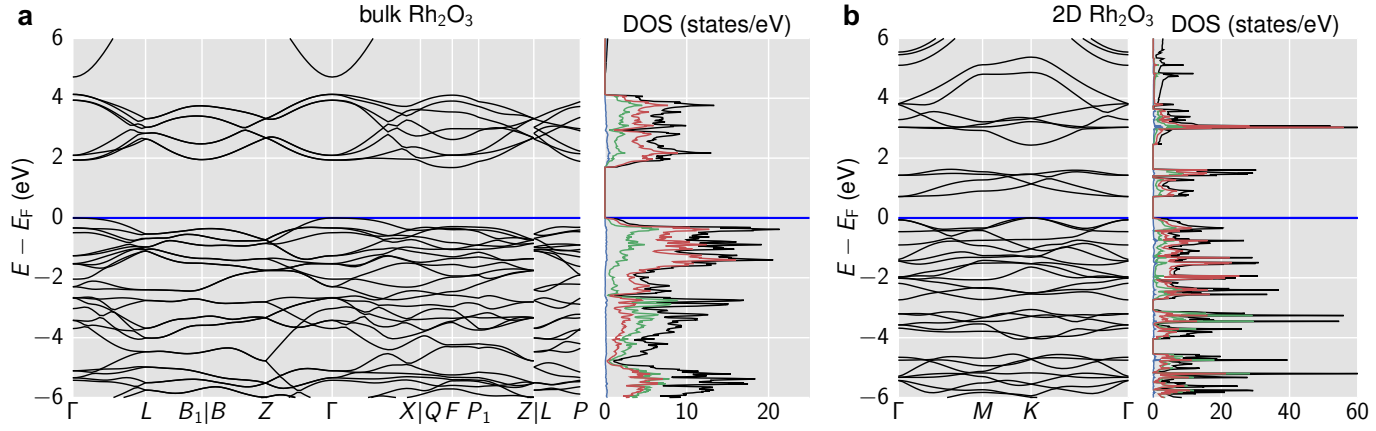

FIG. S10. Bandstructure and density of states for bulk (**a**) and 2D (**b**) Rh_2O_3. The energies are aligned at the respective Fermi energy E_F.

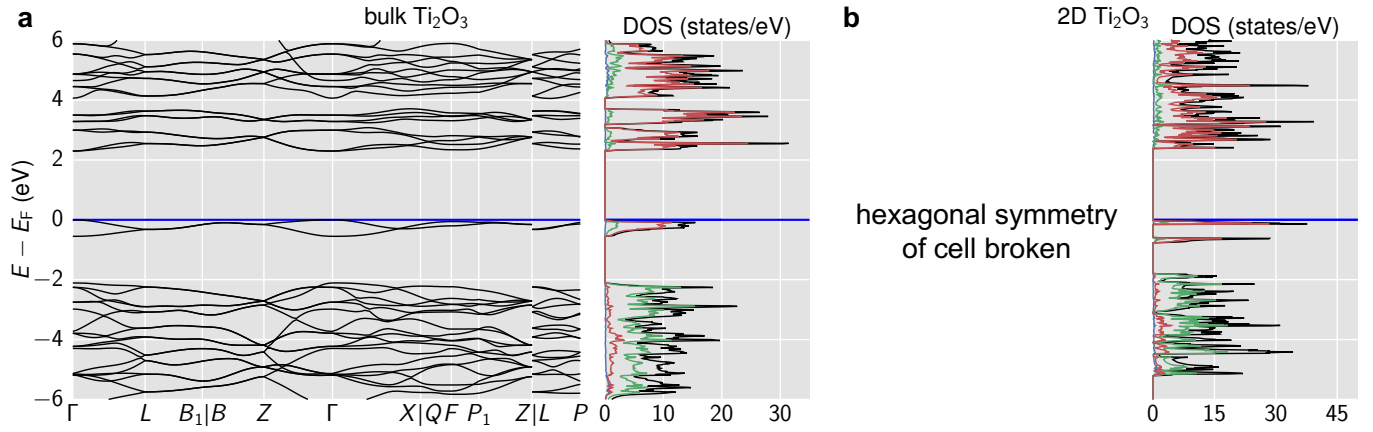

FIG. S11. Bandstructure and density of states for bulk (**a**) and 2D (**b**) Ti_2O_3. The energies are aligned at the respective Fermi energy E_F.

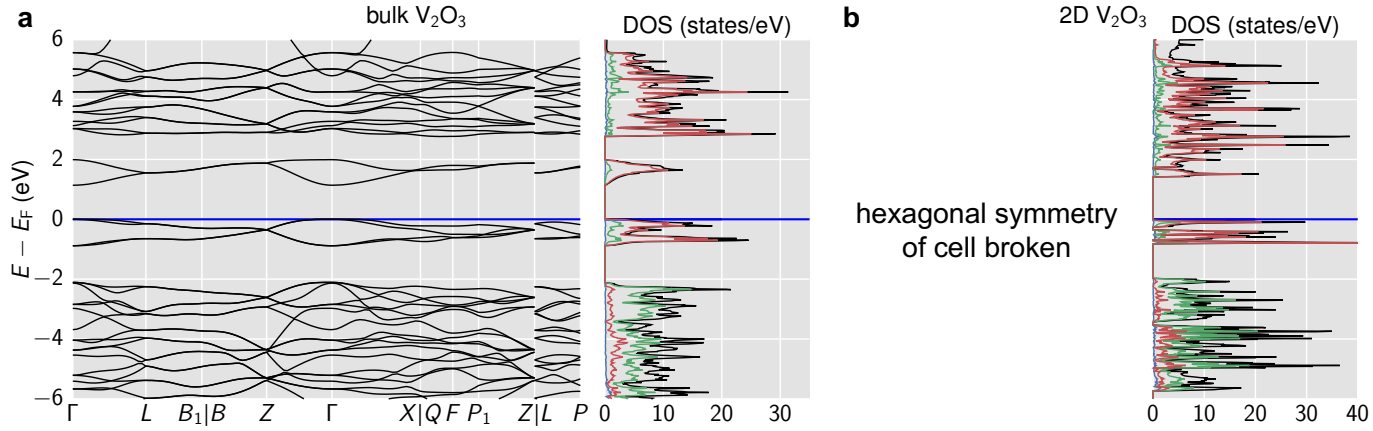

FIG. S12. Bandstructure and density of states for bulk (**a**) and 2D (**b**) V_2O_3. The energies are aligned at the respective Fermi energy E_F.

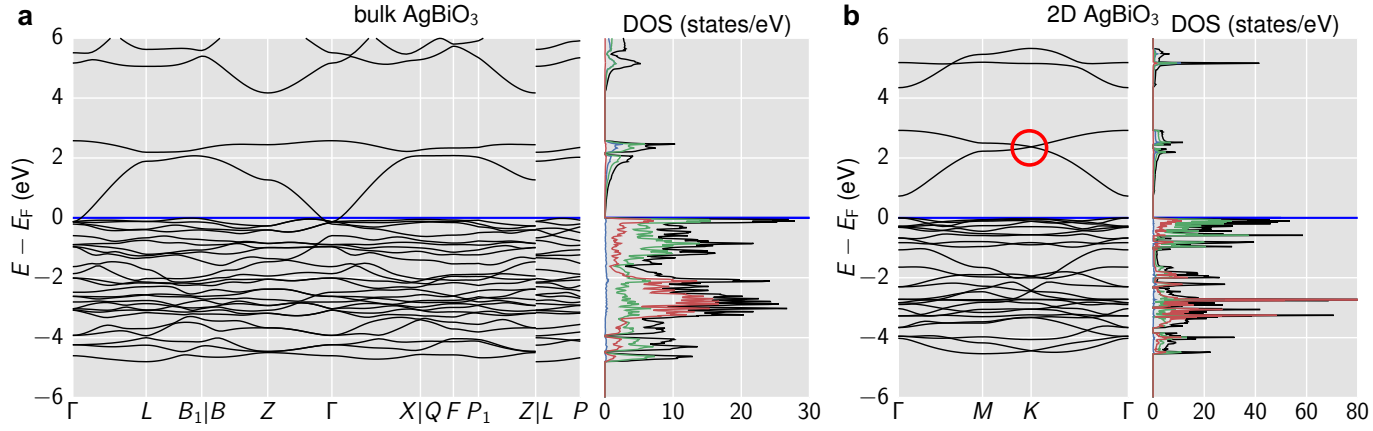

FIG. S13. Bandstructure and density of states for bulk (**a**) and 2D (**b**) $AgBiO_3$. The energies are aligned at the respective Fermi energy E_F. A linear band crossing at the K-point is highlighted by the circle.

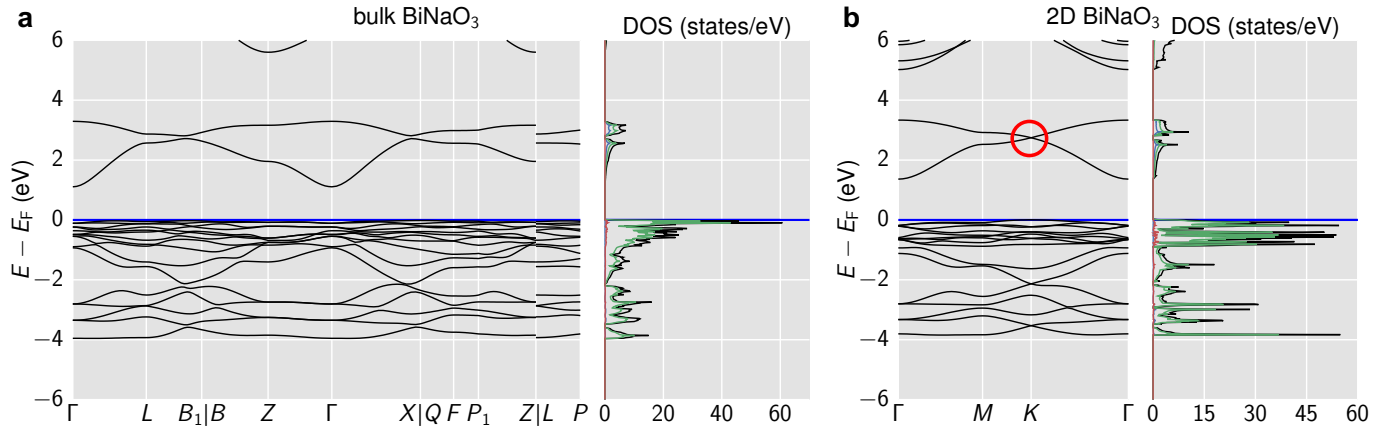

FIG. S14. Bandstructure and density of states for bulk (**a**) and 2D (**b**) $BiNaO_3$. The energies are aligned at the respective Fermi energy E_F. A linear band crossing at the K-point is highlighted by the circle.

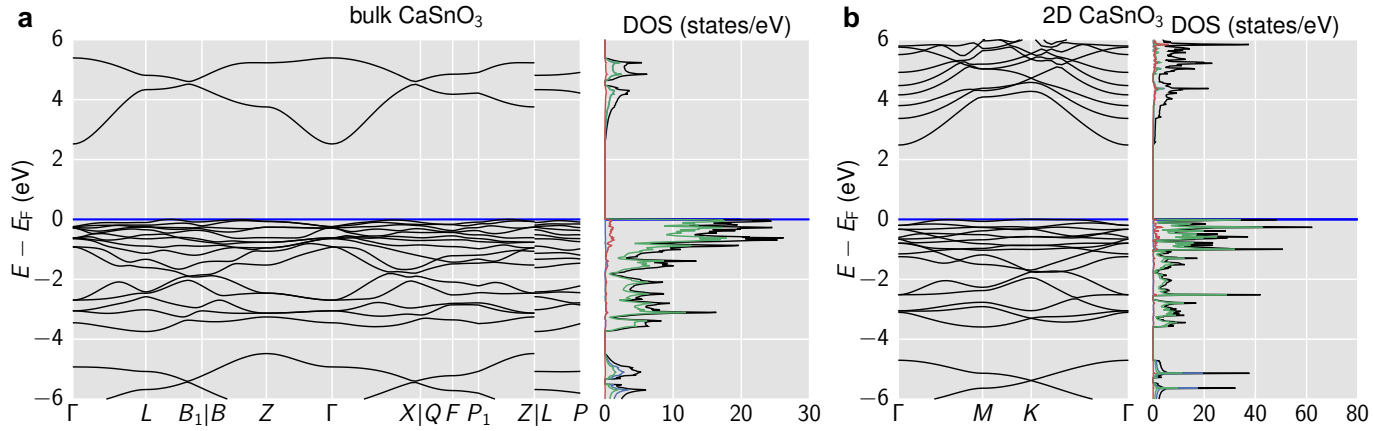

FIG. S15. Bandstructure and density of states for bulk (**a**) and 2D (**b**) $CaSnO_3$. The energies are aligned at the respective Fermi energy E_F.

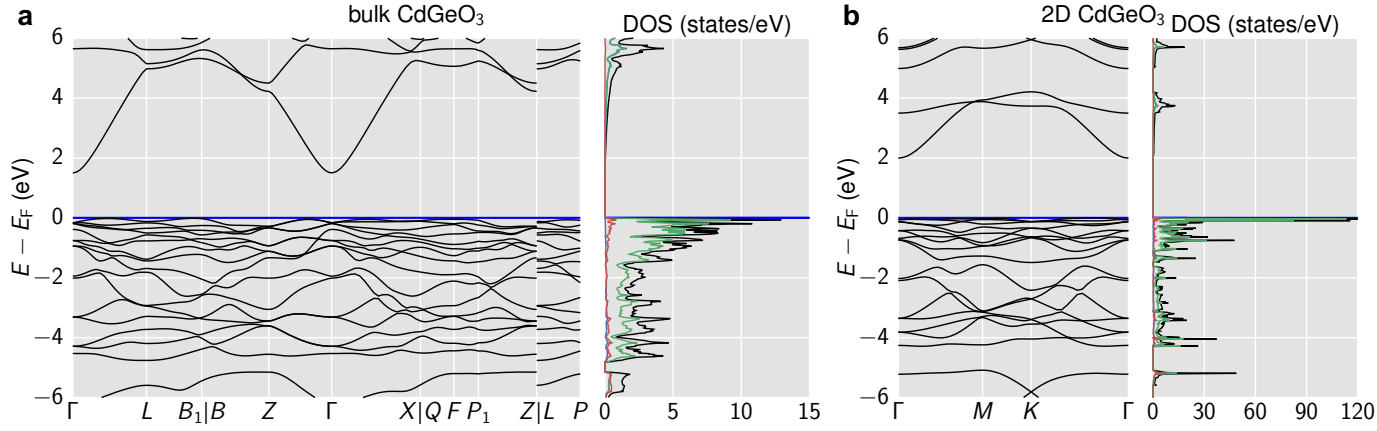

FIG. S16. Bandstructure and density of states for bulk (**a**) and 2D (**b**) $CdGeO_3$. The energies are aligned at the respective Fermi energy E_F.

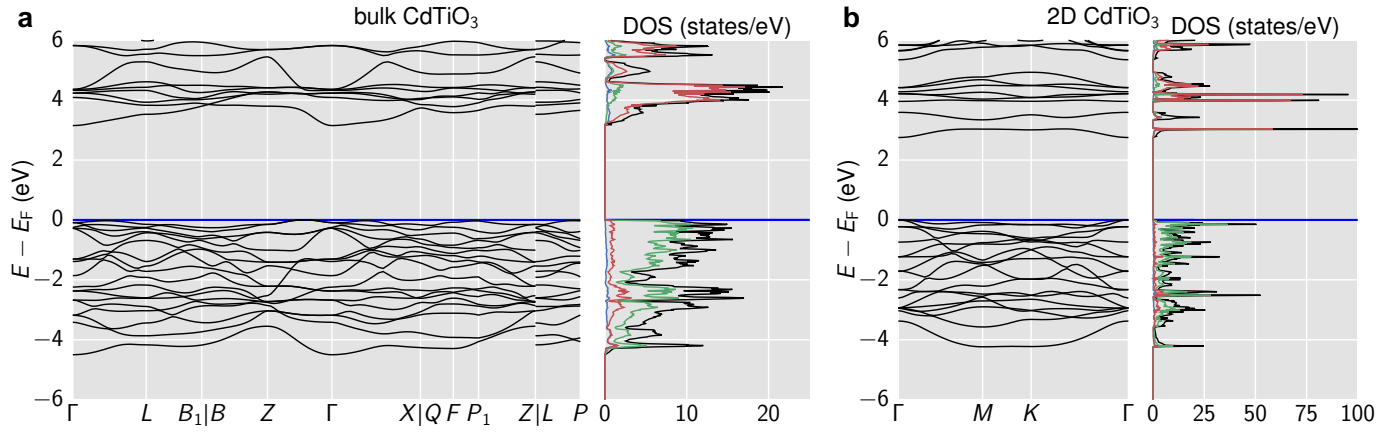

FIG. S17. Bandstructure and density of states for bulk (**a**) and 2D (**b**) $CdTiO_3$. The energies are aligned at the respective Fermi energy E_F.

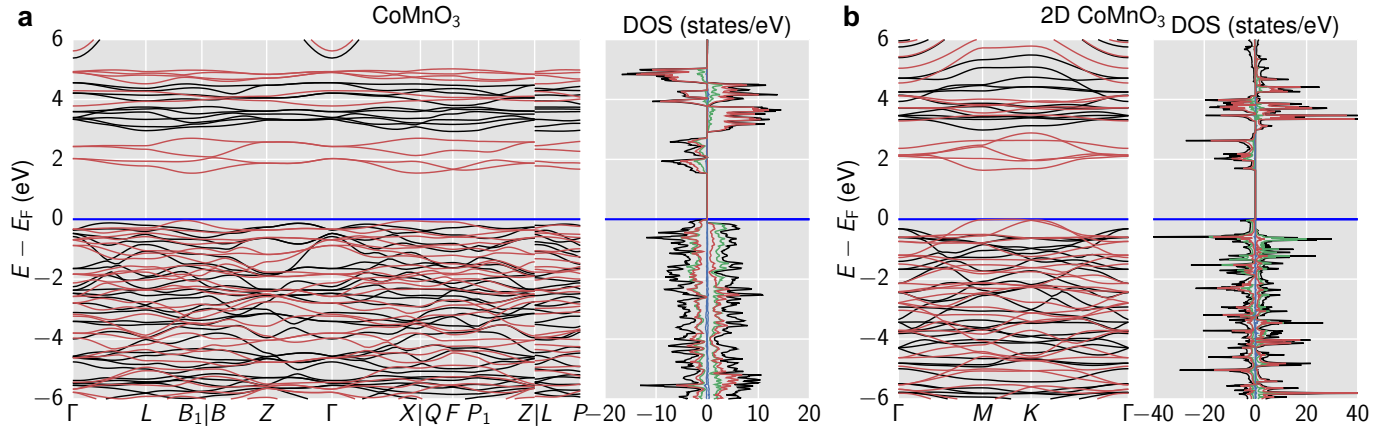

FIG. S18. Bandstructure and density of states for bulk (**a**) and 2D (**b**) $CoMnO_3$. The energies are aligned at the respective Fermi energy E_F. For the spin polarized bandstructure, majority spin bands (positive DOS) are indicated in black while minority spin bands (negative DOS) are in red.

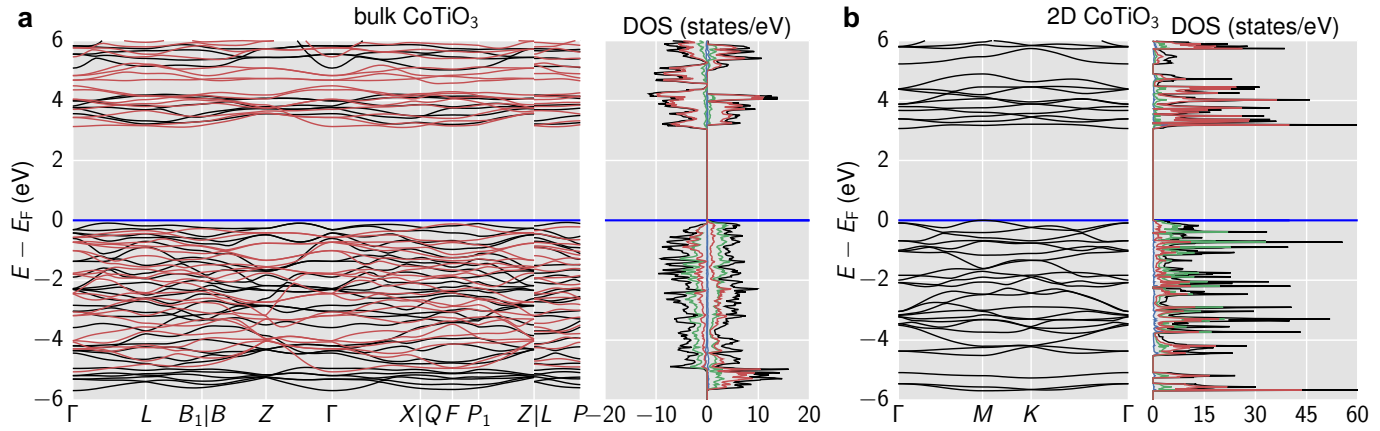

FIG. S19. Bandstructure and density of states for bulk (**a**) and 2D (**b**) $CoTiO_3$. The energies are aligned at the respective Fermi energy E_F. For the spin polarized bandstructure, majority spin bands (positive DOS) are indicated in black while minority spin bands (negative DOS) are in red.

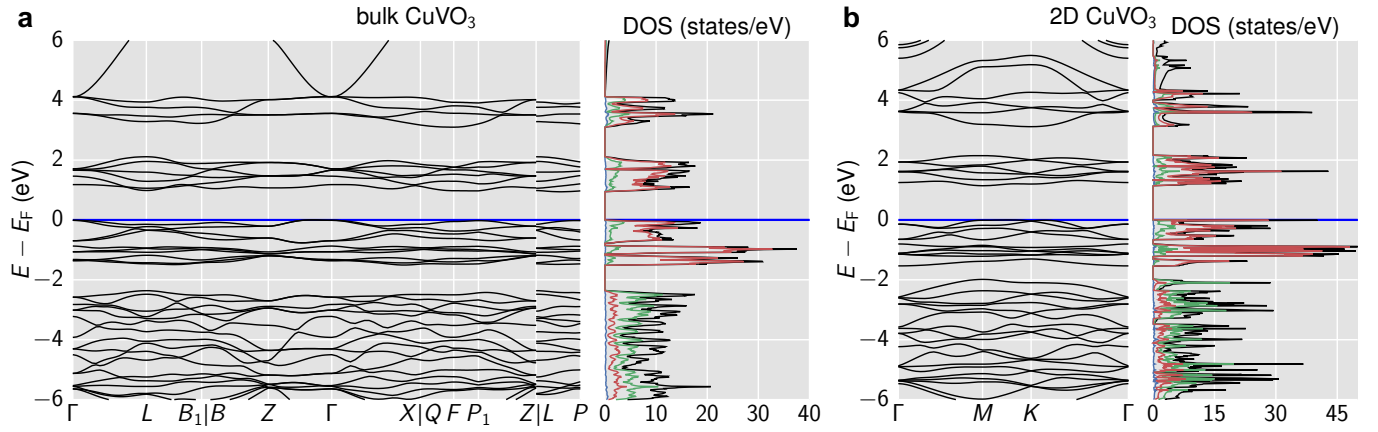

FIG. S20. Bandstructure and density of states for bulk (**a**) and 2D (**b**) $CuVO_3$. The energies are aligned at the respective Fermi energy E_F.

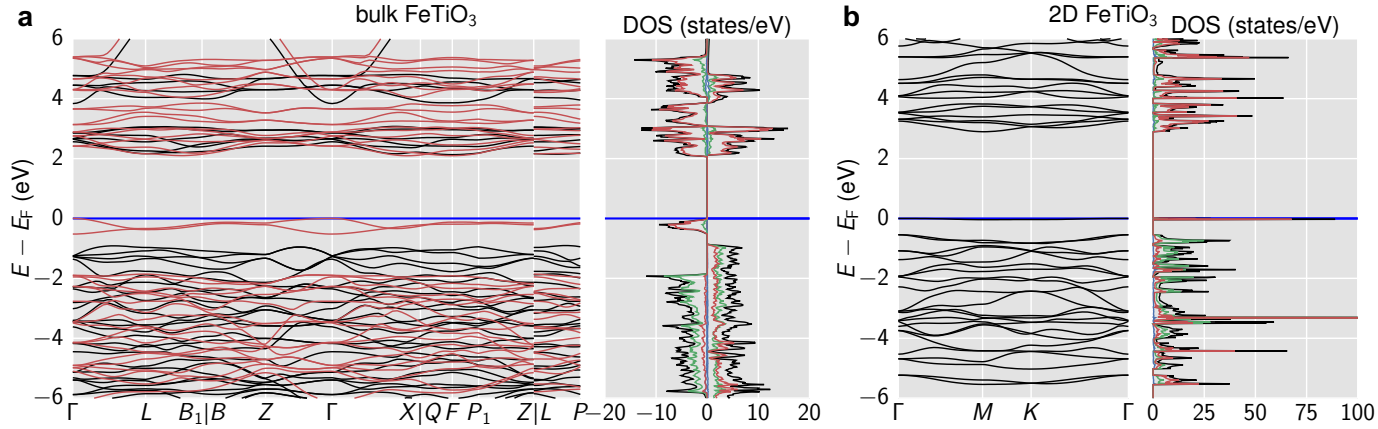

FIG. S21. Bandstructure and density of states for bulk (**a**) and 2D (**b**) $FeTiO_3$. The energies are aligned at the respective Fermi energy E_F. For the spin polarized bandstructure, majority spin bands (positive DOS) are indicated in black while minority spin bands (negative DOS) are in red.

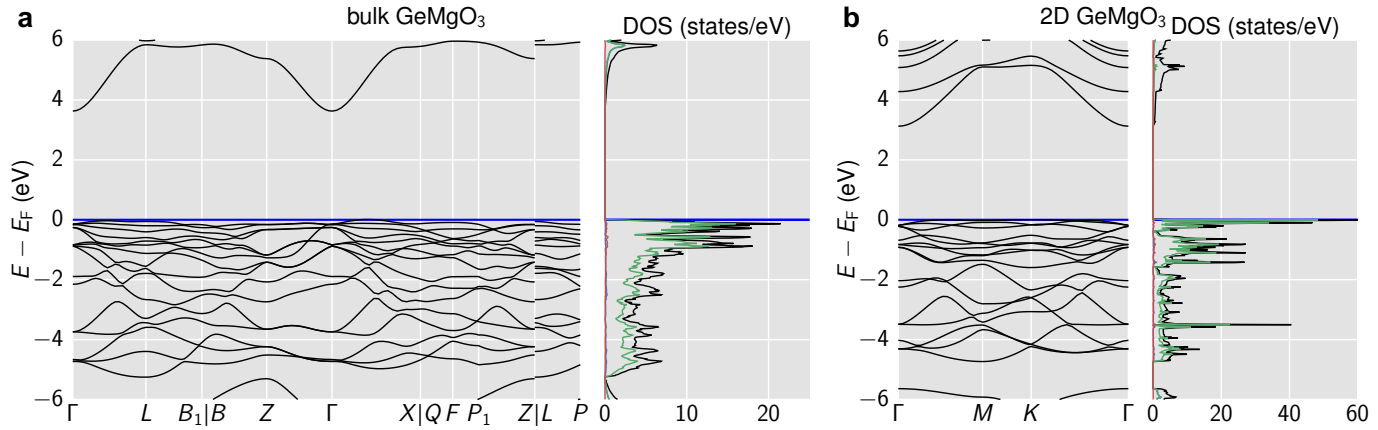

FIG. S22. Bandstructure and density of states for bulk (**a**) and 2D (**b**) $GeMgO_3$. The energies are aligned at the respective Fermi energy E_F.

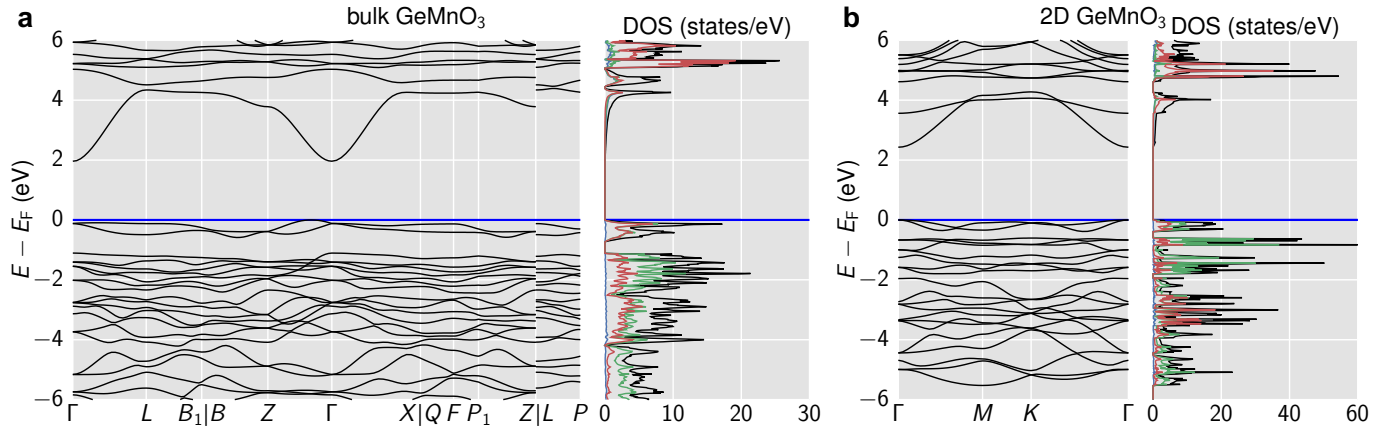

FIG. S23. Bandstructure and density of states for bulk (**a**) and 2D (**b**) $GeMnO_3$. The energies are aligned at the respective Fermi energy E_F.

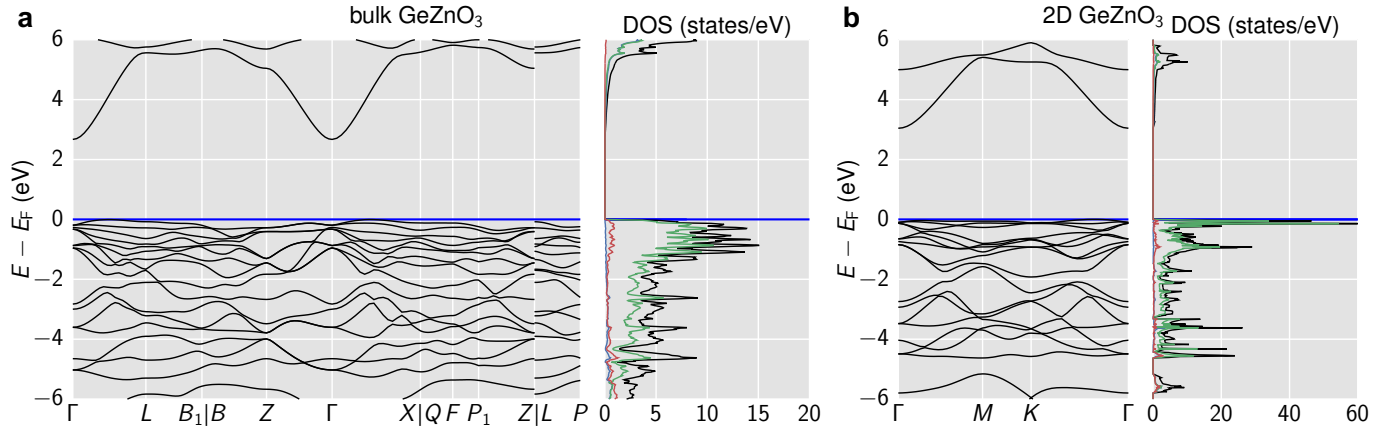

FIG. S24. Bandstructure and density of states for bulk (**a**) and 2D (**b**) $GeZnO_3$. The energies are aligned at the respective Fermi energy E_F.

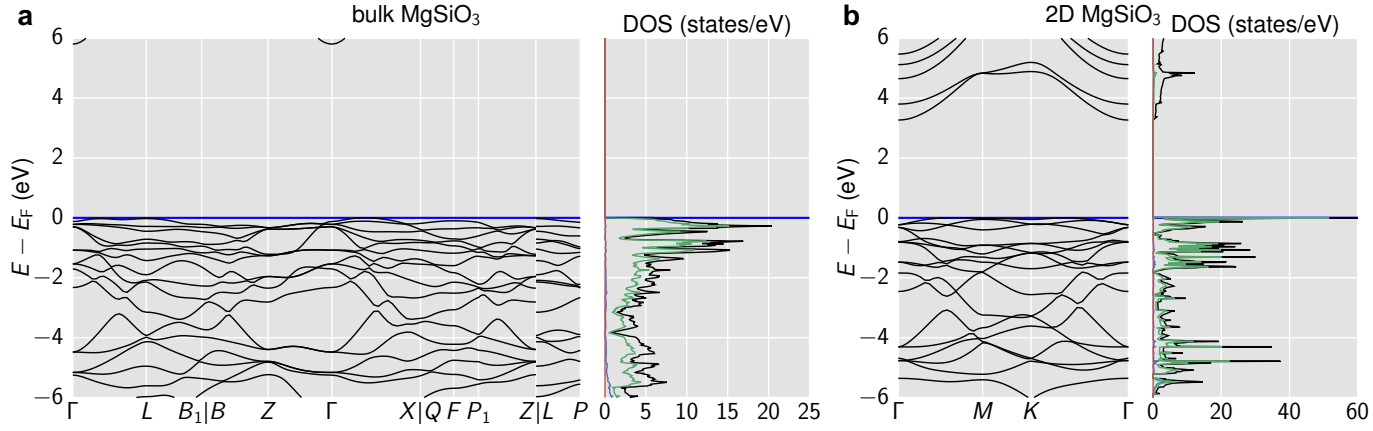

FIG. S25. Bandstructure and density of states for bulk (**a**) and 2D (**b**) $MgSiO_3$. The energies are aligned at the respective Fermi energy E_F.

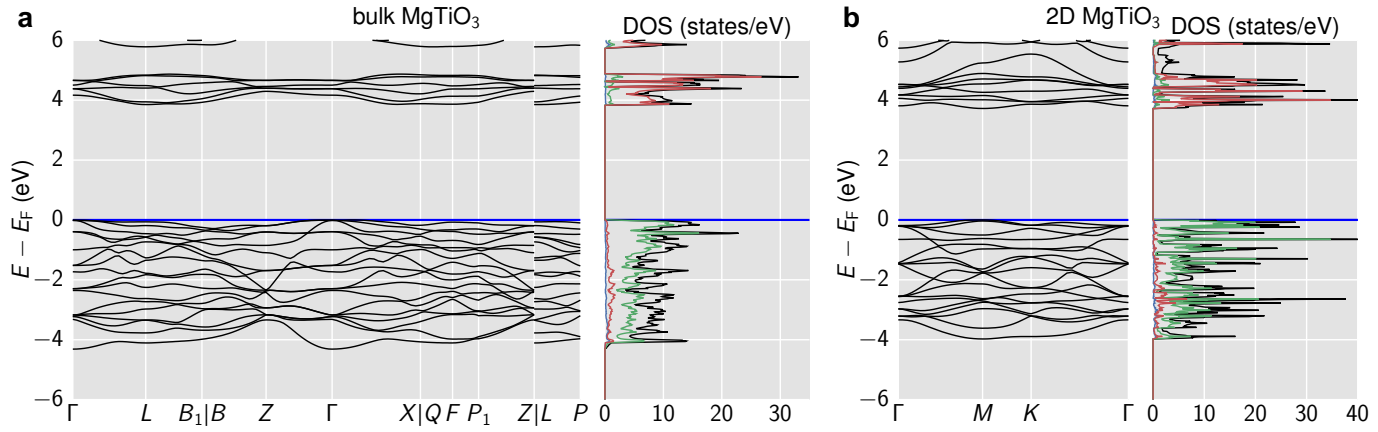

FIG. S26. Bandstructure and density of states for bulk (**a**) and 2D (**b**) $MgTiO_3$. The energies are aligned at the respective Fermi energy E_F.

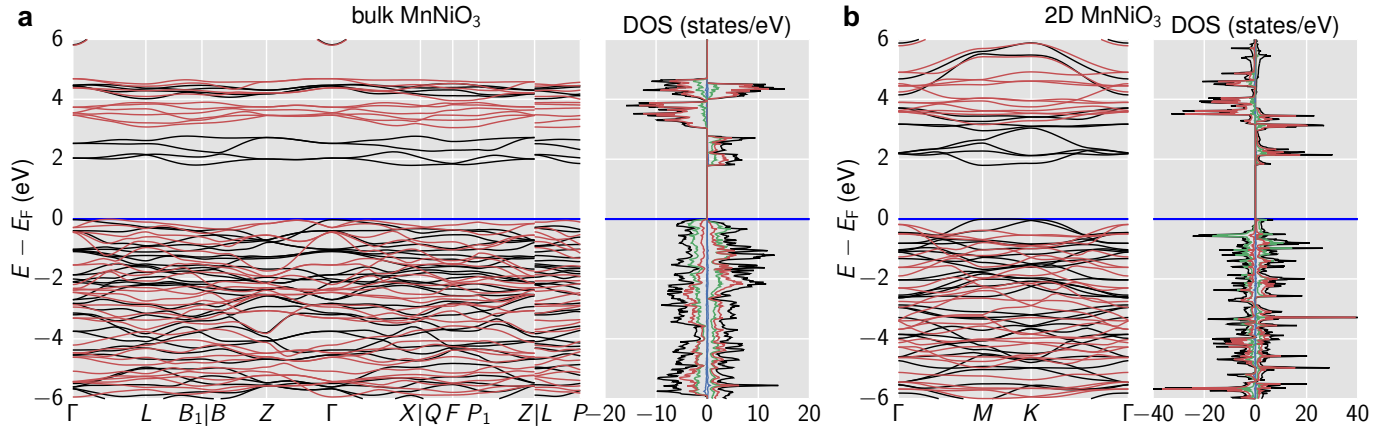

FIG. S27. Bandstructure and density of states for bulk (**a**) and 2D (**b**) $MnNiO_3$. The energies are aligned at the respective Fermi energy E_F. For the spin polarized bandstructure, majority spin bands (positive DOS) are indicated in black while minority spin bands (negative DOS) are in red.

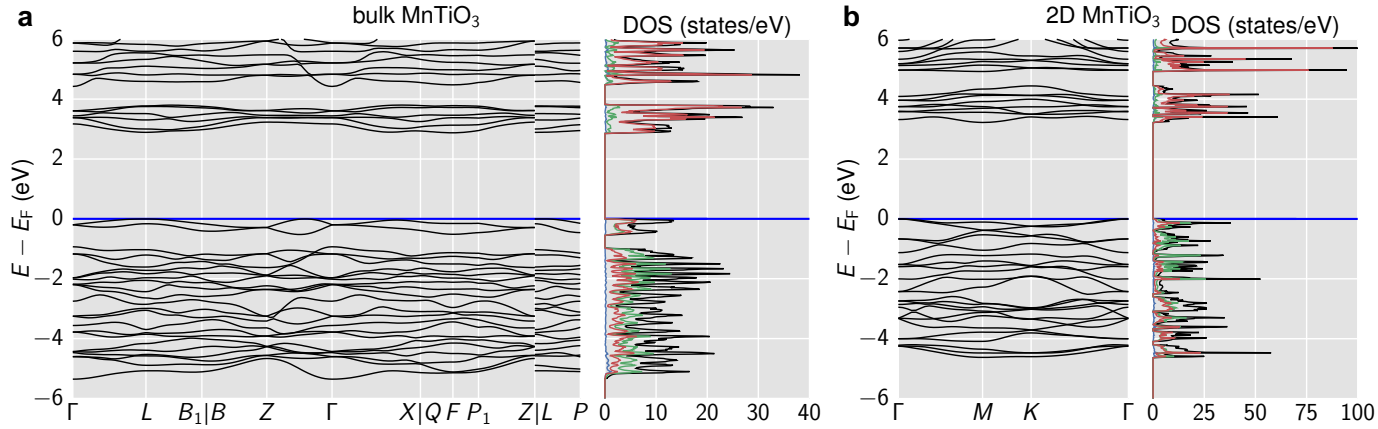

FIG. S28. Bandstructure and density of states for bulk (**a**) and 2D (**b**) $MnTiO_3$. The energies are aligned at the respective Fermi energy E_F.

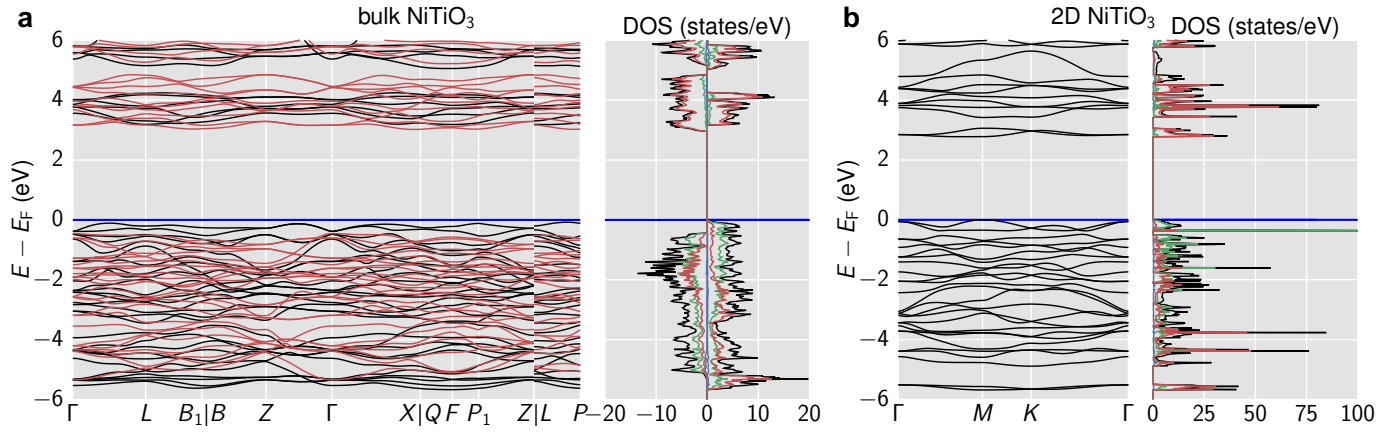

FIG. S29. Bandstructure and density of states for bulk (**a**) and 2D (**b**) $NiTiO_3$. The energies are aligned at the respective Fermi energy E_F. For the spin polarized bandstructure, majority spin bands (positive DOS) are indicated in black while minority spin bands (negative DOS) are in red.

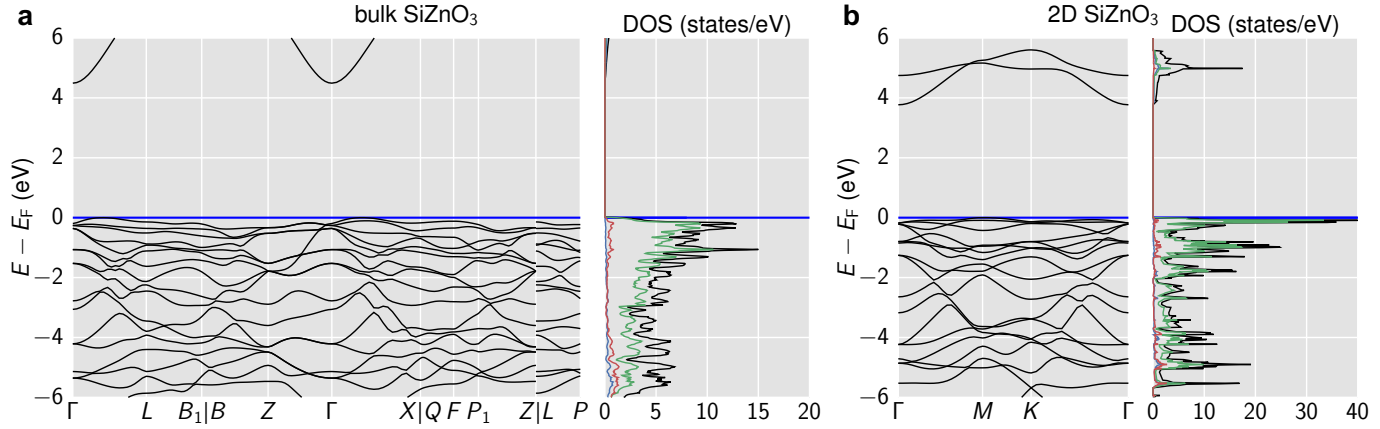

FIG. S30. Bandstructure and density of states for bulk (**a**) and 2D (**b**) $SiZnO_3$. The energies are aligned at the respective Fermi energy E_F.

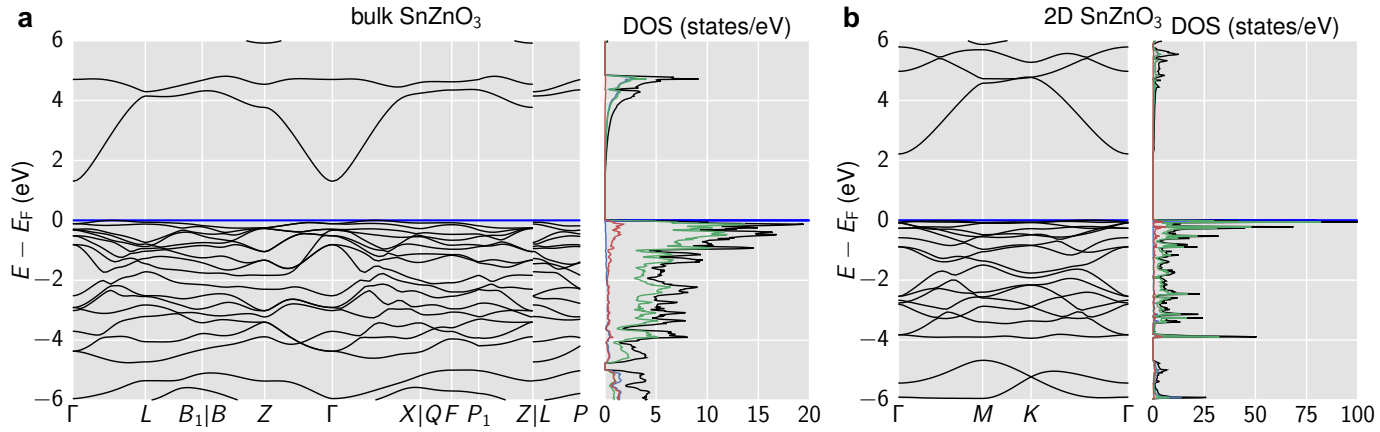

FIG. S31. Bandstructure and density of states for bulk (**a**) and 2D (**b**) $SnZnO_3$. The energies are aligned at the respective Fermi energy E_F.

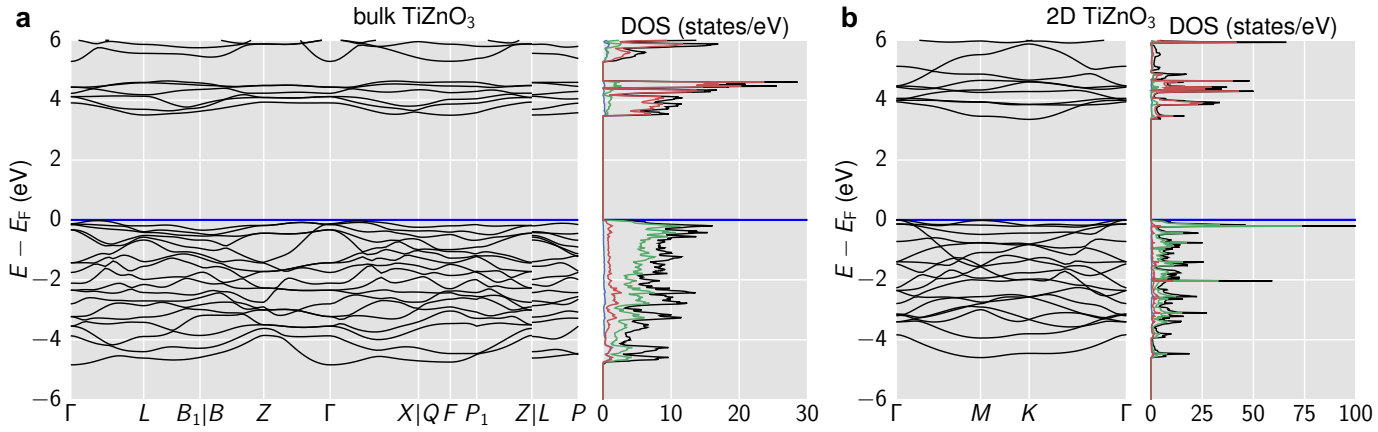

FIG. S32. Bandstructure and density of states for bulk (**a**) and 2D (**b**) $TiZnO_3$. The energies are aligned at the respective Fermi energy E_F.

VI. Tables with numerical data

TABLE I: **Exfoliation energies for binaries.** Exfoliation energies for the binary systems calculated with different functionals from only a static electronic calculation, a relaxation of the ionic positions as well as also relaxing the (in-plane) cell parameters of the 2D materials. All values are in eV/Å^2.

formula	LDA			PBE			PBE+U			SCAN		
	static	rel. ions	rel. ions and cell	static	rel. ions	rel. ions and cell	static	rel. ions	rel. ions and cell	static	rel. ions	rel. ions and cell
Al_2O_3	0.500	0.272	0.264	0.434	0.208	0.200	0.434	0.208	0.200	0.504	0.260	0.250
Cr_2O_3	0.408	0.236	0.208	0.304	0.168	0.158	0.326	0.190	0.188	0.390	0.246	0.242
Fe_2O_3	0.314	0.212	0.184	0.230	0.150	0.108	0.260	0.144	0.140	0.270	0.170	0.164
Ga_2O_3	0.342	0.180	0.176	0.274	0.124	0.120	0.284	0.128	0.124	0.340	0.170	0.164
In_2O_3	0.276	0.182	0.178	0.224	0.134	0.130	0.232	0.138	0.134	0.272	0.176	0.170
Rh_2O_3	0.318	0.212	0.212	0.234	0.134	0.134	0.276	0.168	0.168	0.308	0.196	0.196
Ti_2O_3	0.352	0.198	0.194	0.266	0.130	0.124	0.254	0.124	0.122	0.282	0.162	0.154
V_2O_3	0.414	0.212	0.204	0.290	0.128	0.116	0.282	0.176	0.146	0.296	0.186	0.162

TABLE II: **Exfoliation energies for ternaries.** Exfoliation energies for the ternary systems calculated with PBE+U and SCAN for fully relaxing all systems, *i.e.* the ionic positions and the (in-plane) cell parameters. The data for both the energetically preferred (more stab.) and the less preferred (less stab.) cation termination are given. All values are in eV/Å^2.

formula	PBE+U		SCAN		formula	PBE+U		SCAN	
	more stab.	less stab.	more stab.	less stab.		more stab.	less stab.	more stab.	less stab.
$AgBiO_3$	0.018	0.116	0.034	0.078	$GeMnO_3$	0.082	0.146	0.056	0.100
$BiNaO_3$	0.028	0.210	0.040	0.234	$GeZnO_3$	0.052	0.174	0.080	0.218
$CaSnO_3$	0.090	0.190	0.116	0.248	$MgSiO_3$	0.126	0.172	0.160	0.222
$CdGeO_3$	0.066	0.142	0.096	0.190	$MgTiO_3$	0.112	0.246	0.154	0.266
$CdTiO_3$	0.072	0.230	0.108	0.248	$MnNiO_3$	0.088	0.200	0.130	0.262
$CoMnO_3$	0.084	0.194	0.130	0.200	$MnTiO_3$	0.084	0.238	0.112	0.252
$CoTiO_3$	0.082	0.246	0.112	0.270	$NiTiO_3$	0.094	0.244	0.138	0.264
$CuVO_3$	0.032	0.182	0.066	0.212	$SiZnO_3$	0.062	0.198	0.092	0.240
$FeTiO_3$	0.056	0.206	0.088	0.228	$SnZnO_3$	0.040	0.204	0.066	0.268
$GeMgO_3$	0.114	0.164	0.146	0.214	$TiZnO_3$	0.054	0.254	0.094	0.272

TABLE III: **Structural properties for binaries.** In plane lattice constants and slab thicknesses for the relaxed binary 2D systems and as cut from the corresponding bulk structure for PBE+U and SCAN. All values are in Å.

formula	PBE+U				SCAN			
	a_{2D}	a_{bulk}	d_{2D}	d_{bulk}	a_{2D}	a_{bulk}	d_{2D}	d_{bulk}
Al_2O_3	4.922	4.807	2.721	3.877	4.864	4.749	2.725	3.839
Cr_2O_3	5.145	5.060	3.112	4.206	5.023	4.943	3.146	4.188

TABLE III. (*continued*)

formula	PBE+U				SCAN			
	a_{2D}	a_{bulk}	d_{2D}	d_{bulk}	a_{2D}	a_{bulk}	d_{2D}	d_{bulk}
Fe_2O_3	5.195	5.091	3.025	4.063	5.113	5.003	2.570	3.951
Ga_2O_3	5.129	5.032	2.762	3.918	5.080	4.982	2.753	3.894
In_2O_3	5.657	5.543	3.071	4.210	5.623	5.510	3.056	4.141
Rh_2O_3	5.153	5.175	3.435	4.255	5.106	5.138	3.424	4.179
Ti_2O_3	5.358	5.346	2.897	4.132	5.209	5.105	2.655	4.277
V_2O_3	5.250	5.108	2.721	4.217	5.197	4.964	2.474	4.290

TABLE IV: **Structural properties for ternaries.** In plane lattice constants and slab thicknesses for the relaxed ternary 2D systems and as cut from the corresponding bulk structure for PBE+U and SCAN for the energetically preferred cation termination. All values are in Å.

formula	PBE+U				SCAN			
	a_{2D}	a_{bulk}	d_{2D}	d_{bulk}	a_{2D}	a_{bulk}	d_{2D}	d_{bulk}
$AgBiO_3$	5.802	5.729	3.254	4.312	5.774	5.700	2.977	4.092
$BiNaO_3$	5.725	5.674	3.805	4.469	5.643	5.591	3.803	4.377
$CaSnO_3$	5.659	5.637	3.678	4.277	5.516	5.509	3.696	4.216
$CdGeO_3$	5.229	5.190	3.297	4.037	5.159	5.120	3.275	4.010
$CdTiO_3$	5.394	5.337	3.279	4.103	5.300	5.250	3.261	4.074
$CoMnO_3$	5.072	5.010	2.971	3.854	4.945	4.882	3.004	3.866
$CoTiO_3$	5.247	5.153	2.960	4.007	5.164	5.044	2.732	3.961
$CuVO_3$	5.101	4.997	2.966	4.014	5.030	4.918	2.877	4.001
$FeTiO_3$	5.276	5.212	2.930	4.018	5.159	5.076	2.907	4.098
$GeMgO_3$	5.084	5.013	3.039	3.922	5.014	4.943	3.043	3.880
$GeMnO_3$	5.146	5.096	3.156	3.986	4.813	5.012	4.036	4.473
$GeZnO_3$	5.047	4.989	2.774	3.707	5.026	4.973	2.801	3.660
$MgSiO_3$	4.838	4.783	3.056	3.825	4.783	4.726	3.052	3.805
$MgTiO_3$	5.242	5.140	3.031	4.040	5.150	5.050	3.031	4.007
$MnNiO_3$	5.038	4.977	3.032	3.943	4.919	4.867	3.080	3.937
$MnTiO_3$	5.304	5.227	3.105	4.070	5.202	5.114	2.986	4.040
$NiTiO_3$	5.215	5.118	3.050	4.139	5.111	5.018	3.060	4.124
$SiZnO_3$	4.803	4.757	2.833	3.626	4.792	4.744	2.900	3.668
$SnZnO_3$	5.475	5.364	2.738	3.933	5.391	5.301	2.740	3.812
$TiZnO_3$	5.205	5.112	2.790	3.859	5.164	5.072	2.839	3.864

TABLE V. **Magnetic properties for binaries with SCAN.** Energetically preferred magnetic ordering type, energy difference $\Delta E = E_{AFM} - E_{FM}$ between AFM and FM ordering in eV/formula unit, and absolute magnetic moments for the different sublattices in μ_B for the bulk and corresponding [001] facets as calculated with SCAN. NM stands for non-magnetic.

formula	mag. order type		ΔE		μ_{bulk}	μ_{2D}	
	bulk	2D	bulk	2D		inner	outer
Cr_2O_3	AFM	AFM	−0.150	−0.044	2.73	2.72	2.73
Fe_2O_3	AFM	AFM	−0.801	−0.323	3.93	3.68	3.57
Ti_2O_3	NM	FM	-	0.118	-	0.75	0.15
V_2O_3	FM	AFM	0.012	−0.247	1.89	2.21	0.03

TABLE VI. **Magnetic properties for ternaries with SCAN.** Energetically preferred magnetic ordering type, energy difference $\Delta E = E_{AFM} - E_{FM}$ between AFM and FM ordering in eV/formula unit, and absolute magnetic moments for the inner and outer magnetic ions of the slab in μ_B for the bulk and corresponding [001] facets as calculated with SCAN. The A element is the first cation species in the formula while the B element corresponds to the second. The terminating elements of the slabs (outer ions) are underlined.

formula	mag. order type		ΔE		μ_{bulk}		μ_{2D}	
	bulk	2D	bulk	2D	A el.	B el.	inner	outer
$\underline{Co}MnO_3$	AFM	AFM	−0.386	−0.338	2.50	2.62	2.92	2.48
$\underline{Co}TiO_3$	FM	AFM	0.014	−0.172	2.58	0.09	0.00	2.43
$\underline{Fe}TiO_3$	FM	AFM	0.102	−0.018	3.72	0.08	0.02	3.53
$\underline{Ge}MnO_3$	AFM	FM	−0.061	0.004	0.01	4.49	2.71	0.02
$Mn\underline{Ni}O_3$	AFM	AFM	−0.244	−0.279	2.63	1.56	2.73	1.53
$\underline{Mn}TiO_3$	AFM	AFM	−0.049	−0.038	4.42	0.02	0.00	4.36
$\underline{Ni}TiO_3$	AFM	AFM	−0.002	−0.003	1.64	0.03	0.01	1.61

REFERENCES

[1] R. Zacharia, H. Ulbricht, and T. Hertel, *Interlayer cohesive energy of graphite from thermal desorption of polyaromatic hydrocarbons*, Phys. Rev. B **69**, 155406 (2004).

[2] N. Mounet, M. Gibertini, P. Schwaller, D. Campi, A. Merkys, A. Marrazzo, T. Sohier, I. E. Castelli, A. Cepellotti, G. Pizzi, and N. Marzari, *Two-dimensional materials from high-throughput computational exfoliation of experimentally known compounds*, Nat. Nanotechnol. **13**, 246–252 (2018).

[3] Y. Zhang, J. W. Furness, B. Xiao, and J. Sun, *Subtlety of TiO2 phase stability: Reliability of the density functional theory predictions and persistence of the self-interaction error*, J. Chem. Phys. **150**, 014105 (2019).